Modal Propagation and Crosstalk Analysis in Coupled Graphene Nanoribbons

Rodolfo Araneo, *Senior Member, IEEE*, Paolo Burghignoli, *Senior Member, IEEE*, Giampiero Lovat, *Member, IEEE*, and George W. Hanson, *Fellow, IEEE*

***Abstract*—A full-wave analysis of the fundamental quasi-TEM modes supported by multiple graphene nanoribbons above a ground plane is presented, aimed at characterizing crosstalk in graphene multiconductor lines. A method-of-moments discretization of the relevant electric-field integral equation is performed. Assuming first a local scalar conductivity, an efficient spatial-domain approach with subsectional basis functions is assuming first a local scalar conductivity, a spatial-domain approach with subsectional basis functions is developed. This allows for the efficient treatment of nanoribbons with wide transverse separations, and can be expanded to include in the simulation model spatial nonuniformity of the graphene conductivity. This spatial-domain formulation is then extended to treat the case of weakly nonlocal conductivity, via an original integro-differential approach derived by approximating a recent full spectral graphene conductivity model in the limit of low wavenumbers. Numerical results are provided for propagation constants and characteristic impedances of two identical coupled graphene nanoribbons; on this basis, a crosstalk analysis is performed by means of the modal decomposition method.**

***Index Terms*—Crosstalk, graphene, multiconductor transmission lines, nanoribbon, spatial dispersion.**

I. Introduction

STRIP transmission lines with submicrometric transverse dimensions based on graphene [graphene nanoribbons, (GNRs)] are emerging as candidates for the realization of future interconnects in carbon-based nanoelectronic circuits [1], and various approaches have been adopted so far for the assessment of their propagation features [2]–[8].

It has been demonstrated that the performance of GNR interconnects on the scale of nanometers are comparable to even the most optimistic projections for copper interconnects at the same scale; however, their development for future large-scale integrated circuits is still challenging due to several difficulties in fabrication processes, which are less practical or more expensive. In addition, when moving to the terahertz, regime, the absence of cheap and convenient sources for radiation adds further difficulties (quantum-cascade laser and traveling-wave tube amplifier are good candidates, but not fully developed yet).

Manuscript received November 2, 2014; revised January 15, 2015; accepted February 19, 2015. Date of publication March 19, 2015; date of current version August 13, 2015. This paper is an expanded version from the 2014 IEEE International Symposium on EMC, Raleigh, NC, USA, August 3–8, 2014.

R. Araneo and G. Lovat are with the Department of Astronautical, Electrical, and Energetic Engineering, Sapienza University of Rome, 00185 Rome, Italy (e-mail: rodolfo.araneo@uniroma1.it; giampiero.lovat@uniroma1.it).

P. Burghignoli is with the Department of Information Engineering, Electronics and Telecommunications, Sapienza University of Rome, 00185 Rome, Italy (e-mail: burghignoli@die.uniroma1.it).

G. W. Hanson is with the Department of Electrical Engineering and Computer Science, University of Wisconsin-Milwaukee, Milwaukee, WI 53211 USA (e-mail: george@uwm.edu).

Color versions of one or more of the figures in this paper are available online at http://ieeexplore.ieee.org.

Digital Object Identifier 10.1109/TEMC.2015.2406072

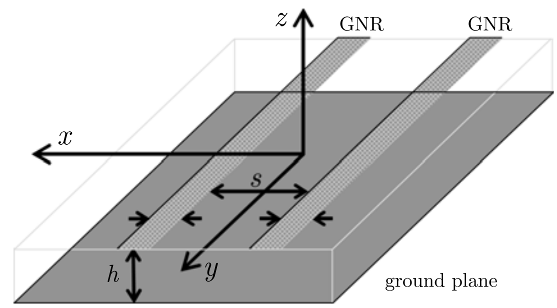

Fig. 1. Coupled GNRs.

The method-of-moments (MoM) is adopted here for the modal characterization of coupled GNRs, adopting two alternative models for the graphene conductivity. The simplest approach is based on a scalar frequency-dependent but local conductivity; whereas nonlocal effects in GNRs may be nonnegligible, especially in the microwave and millimeter-wave frequency ranges [9], [10], a local model may be still adequate in the Terahertz range [11] and allows for a straightforward implementation in a spatial-domain MoM code. This approach is much better suited than its spectral-domain counterpart for studying multiconductor transmission lines with widely separated ribbons. Furthermore, a spatial-domain approach is the only suitable tool for future modeling of spatially nonuniform graphene conductivity.

Nonlocal effects in graphene can be modeled through a spectral domain dyadic conductivity, recently obtained in a semiclassical framework using the Bhatnagar–Gross–Krook (BGK) approximation of the Boltzmann transport equation [10]. Starting from such a representation, an approximate space-domain integro-differential equation is derived for the current density on a GNR, valid in the limit of low wavenumbers. The equation is then discretized with the method of moments adopting subsectional basis functions and enforcing the correct behavior of the transverse current at the edges. The resulting formulation can be used for modeling weakly nonlocal effects in coupled GNRs. It is worth noting that, in principle, the spatial-domain formulation may be extended to a strongly nonlocal case if one could formulate the suitable differential equation.

In this paper results are presented, based on such spatial-domain formulations, for dispersion and attenuation properties of the two fundamental (even and odd) quasi-TEM modes supported by two coupled GNRs (see Fig. 1); the case of identical GNRs on an air substrate is considered for simplicity, although

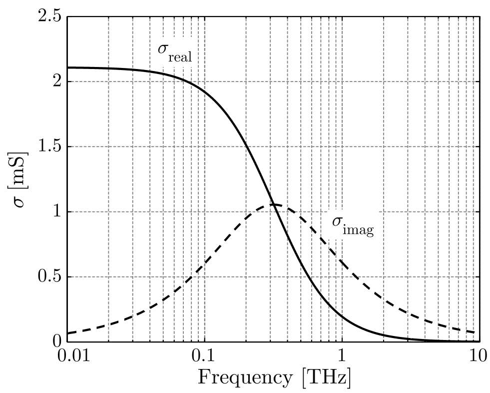

Fig. 2. Real and imaginary parts of graphene intraband (Drude) conductivity.

the analysis can be extended in a straightforward way to multiple GNRs having different widths embedded in a general multilayered dielectric environment.

The modal characteristic impedance, calculated adopting a power-current definition, is further studied; information on propagation wavenumber and characteristic impedance constitutes the basis for future characterizations of graphene multicondutor lines in network terms [12], [13]. Finally, a crosstalk analysis is conducted by means of the modal decomposition method [14], [15]. Preliminary results have been presented in [16] and [17].

The paper is organized as follows. In Section II, the spatial-domain MoM formulation valid for a local conductivity model is described. In Section III, such a formulation is extended to the weakly nonlocal case. In Section IV, numerical results are presented. Finally, in Section V concluding remarks are offered.

II. Spatial-Domain Formulation: Local Conductivity Model

The structure considered here, shown in Fig. 1, is constituted by a pair of identical GNRs of width w and transverse spacing s placed at a distance h above a perfectly electric conductor ground plane.

Graphene is modeled through a simple local scalar conductivity σ, whose expression [18] is

$$\sigma = -j\frac{e^2 k_{\mathrm{B}} T}{\pi\hbar^2(\omega - j\tau^{-1})}\ln\left[2\left(1+\cosh\left(\frac{\mu}{k_{\mathrm{B}}T}\right)\right)\right] \tag{1}$$

where ω is the radian frequency, τ is the collision time, k_{B} is the Boltzmann constant, T is the absolute temperature, $\hbar$ is the reduced Planck constant, and μ is the graphene chemical potential. In the following, graphene has been modeled assuming $\tau = 0.5$ ps, $T = 300$ K, and $\mu = 0$ eV; the resulting real and imaginary parts of the conductivity are shown in Fig. 2.

The propagation modes of the coupled GNRs are determined by considering an exponential dependence on the longitudinal coordinate y for the modal current density

$$\mathbf{J}(x,y) = \mathbf{j}(x)e^{-jk_y y} \tag{2}$$

where $k_y = \beta - j\alpha$ is the unknown and generally complex modal wavenumber, and $\mathbf{j} = \mathbf{x}_0 j_x + \mathbf{y}_0 j_y$ is the modal current (the z-component of the current is zero due to the 2-D nature of graphene). The translational invariance of the background medium ensures that similar expressions hold for any other modal field or potential quantity; in particular, the tangential electric field on the GNR is $\mathbf{E}_\tau(x,y) = \mathbf{e}_\tau(x)e^{-jk_y y}$. This can be expressed in terms of $\mathbf{j}$ through mixed potentials as

$$\begin{aligned}\mathbf{e}_\tau &= -j\omega\mathbf{a}_\tau - \nabla_\tau\phi\\ &= -j\omega\int_\ell \underline{\tilde{\mathbf{G}}}_A(x-x';k_y)\cdot\mathbf{j}(x')\mathrm{d}x' + \frac{1}{j\omega}\cdot\\ &\quad\cdot\left(\mathbf{x}_0\frac{\partial}{\partial x} - jk_y\mathbf{y}_0\right)\int_\ell \tilde{G}_\Phi(x-x';k_y)\nabla_\tau\cdot\mathbf{j}(x')\mathrm{d}x'\end{aligned} \tag{3}$$

where ℓ is the transverse cross section of the GNRs, whereas $\underline{\tilde{\mathbf{G}}}_A$ and $\tilde{G}_\Phi$ are the vector and scalar potential Green's functions for a line source directed along the y-axis placed above a ground plane and phased with wavenumber k_y

$$\begin{aligned}\underline{\tilde{\mathbf{G}}}_A &= \frac{\mu_0}{4j}\left\{\left[H_0^{(2)}(k_\rho R) - H_0^{(2)}(k_\rho R')\right](\mathbf{u}_x\mathbf{u}_x + \mathbf{u}_y\mathbf{u}_y)\right.\\ &\quad\left. + \left[H_0^{(2)}(k_\rho R) + H_0^{(2)}(k_\rho R')\right]\mathbf{u}_z\mathbf{u}_z\right\}\end{aligned} \tag{4a}$$

$$\tilde{G}_\Phi = \frac{1}{4j\varepsilon_0}\left[H_0^{(2)}(k_\rho R) - H_0^{(2)}(k_\rho R')\right] \tag{4b}$$

where $k_\rho = \sqrt{k_0^2 - k_y^2}$, $R = \sqrt{(x-x')^2 + (z-z')^2}$ and $R' = \sqrt{(x-x')^2 + (z+z')^2}$

By inserting (3) in the constitutive relation for the GNR $\mathbf{j} = \sigma\mathbf{e}_\tau$, written as

$$\frac{1}{\sigma}\mathbf{j} = \mathbf{e}_\tau \tag{5}$$

an integro-differential equation for $\mathbf{j}$ is obtained. This can be discretized with the MoM by letting

$$\mathbf{j}(x) = \sum_{j=1}^{N} I_j \mathbf{\Lambda}_j(x) \tag{6}$$

where $\mathbf{\Lambda}_j$ are suitable subsectional basis functions directed along the *x*- or *y*-axis, and by enforcing a Galerkin testing scheme.

As shown in Fig. 3, standard quadratic B-splines have been adopted: the standard basis function (e.g., basis function #3) is defined over three consecutive segments and has zero derivative at both the ends. Near the strip edges special B-splines (e.g., #2 and #4) defined over two segments are introduced both in the transverse and longitudinal current components, in order to reproduce the derivative of the current with a first-order accuracy. Furthermore, in the longitudinal current component only, special B-splines defined over one interval (e.g., #1 and #5) are introduced to model the possibly divergent behavior of the current near edges.

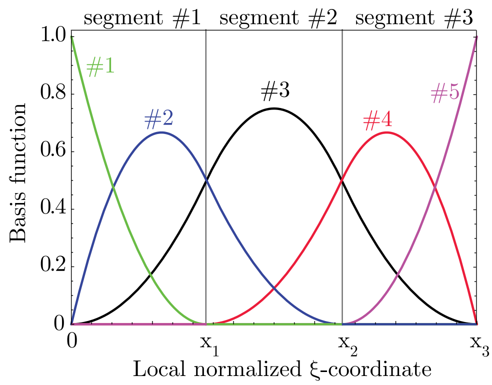

Fig. 3. Basis functions adopted in the MoM discretization of GNRs.

The resulting MoM matrix elements can be expressed as

$$\begin{aligned} Z_{ij}^{\rm loc} = \; & j\omega \int_\ell \int_\ell \boldsymbol{\Lambda}_i(x) \cdot \underline{\tilde{\mathbf{G}}}_A(x-x';k_y) \cdot \boldsymbol{\Lambda}_j(x') \mathrm{d}x\mathrm{d}x' \\ & + \frac{1}{j\omega} \int_\ell \int_\ell \left[\frac{\partial \Lambda_{ix}}{\partial x} + jk_y \Lambda_{iy}(x) \right] \tilde{G}_\Phi(x-x';k_y) \\ & \cdot \left[\frac{\partial \Lambda_{jx}}{\partial x'} - jk_y \Lambda_{jy}(x') \right] \mathrm{d}x\mathrm{d}x' \\ & + \frac{1}{\sigma} \int_\ell \boldsymbol{\Lambda}_i(x) \cdot \boldsymbol{\Lambda}_j(x) \mathrm{d}x \end{aligned} \tag{7}$$

where the superscript loc reminds the local nature of the relevant graphene conductivity model, $i, j = 1, \ldots, N$, and as usual, one del operator has been transferred onto the testing function in the scalar-potential term.

The elements (7) are functions of the unknown modal wavenumber k_y. An approximate dispersion equation is obtained by requiring that the determinant of the MoM matrix vanishes

$$\det\left[\underline{\mathbf{Z}}(k_y)\right] = 0\,. \tag{8}$$

The wavenumber is then determined through a suitable numerical search of the zeros of the determinant in the complex plane of k_y [19], [20]. In particular, the even and odd modes have been searched by enforcing a perfectly conducting magnetic and electric plane on the *yz* plane, respectively. The enforcement of these boundary conditions offers a twofold benefit: only one half of the strip is discretized and the correct propagation constant k_y of the mode under analysis is more easily located in the complex plane since the other mode is not resolved by the MoM matrix.

III. Spatial-Domain Formulation: Weakly Nonlocal Conductivity Model

Let us start with the constitutive relation between surface current density $\mathbf{J}(\mathbf{r})$ and tangential electric field $\mathbf{E}_\tau(\mathbf{r})$ for an ideally infinite graphene sheet, expressed in the spectral domain as

$$\tilde{\mathbf{J}}(\mathbf{q}) = \underline{\boldsymbol{\sigma}}(\mathbf{q}) \cdot \tilde{\mathbf{E}}_\tau(\mathbf{q}) \tag{9}$$

where the tilde indicates spectral quantities and $\mathbf{q}$ is the spectral wavenumber. The spectral conductivity $\underline{\boldsymbol{\sigma}}$ can be expressed in polar coordinates as

$$\begin{aligned} \underline{\boldsymbol{\sigma}}(\mathbf{q}) & \equiv \begin{pmatrix} \sigma_\rho(q) & 0 \\ 0 & \sigma_\phi(q) \end{pmatrix} \\ & = \frac{1}{q^2}\sigma_\rho(q)\mathbf{q}\mathbf{q} + \frac{1}{q^2}\sigma_\phi(q)(\mathbf{z}_0\times\mathbf{q})(\mathbf{z}_0\times\mathbf{q}) \\ & = \sigma_\phi(q)\underline{\mathbf{1}} + \frac{1}{q^2}\left[\sigma_\rho(q) - \sigma_\phi(q)\right]\mathbf{q}\mathbf{q} \end{aligned} \tag{10}$$

where $q = |\mathbf{q}|$ and σ_ϕ, σ_ρ are the transverse and longitudinal conductivities, respectively. These have recently been derived in a semiclassical framework, solving the Boltzmann transport equation under the so-called BGK approximation, which improves on the more common relaxation-time approximation by explicitly enforcing charge conservation [10]; the relevant expressions are

$$\sigma_\phi(q) = \frac{2\sigma}{a}\frac{1-\chi(q)}{q^2}\sigma_\rho(q) = \frac{1}{-2b[1-\chi(q)]+\chi(q)}\sigma_\phi(q) \tag{11}$$

where

$$\chi(q) = \sqrt{1-aq^2} \tag{12}$$

and

$$\begin{aligned} a & = \frac{v_{\rm F}^2}{(\omega - j\tau^{-1})^2}\,, \quad b = \frac{-j\tau^{-1}}{2\omega} \\ \sigma & = -j\frac{e^2 k_{\rm B}T}{\pi\hbar^2(\omega - j\tau^{-1})}\ln\left[2\left(1+\cosh\left(\frac{\mu}{k_{\rm B}T}\right)\right)\right] \end{aligned} \tag{13}$$

where $v_{\rm F} = 10^6$ m/s is the graphene Fermi velocity.

The spectral conductivity (10) can be cast in the compact form

$$\underline{\boldsymbol{\sigma}}(\mathbf{q}) = \sigma_\phi(q)\left[\mathbf{1} + \frac{1}{q^2}\psi(q)\mathbf{q}\mathbf{q}\right] \tag{14}$$

where

$$\psi(q) = \frac{(1+2b)[1-\chi(q)]}{-2b[1-\chi(q)]+\chi(q)} \tag{15}$$

from which its inverse conductivity can easily be calculated as

$$\underline{\boldsymbol{\sigma}}^{-1}(\mathbf{q}) = \frac{1}{\sigma_\phi(q)}\left[\mathbf{1} - \frac{1}{q^2}\frac{\psi(q)}{1+\psi(q)}\mathbf{q}\mathbf{q}\right]. \tag{16}$$

The inverse conductivity (16) can be approximated, in the limit of low wavenumber q, by expanding its terms in a Taylor series of powers of q; by keeping terms up to second order, the result is

$$\underline{\boldsymbol{\sigma}}^{-1}(\mathbf{q}) \simeq \frac{1}{\sigma}\left[\left(1 - \frac{1}{4}aq^2\right)\mathbf{1} - \frac{1}{2}a(1+2b)\mathbf{q}\mathbf{q}\right]. \tag{17}$$

This can be inserted into the constitutive relation for graphene, written in the form

$$\underline{\boldsymbol{\sigma}}^{-1}(\mathbf{q}) \cdot \tilde{\mathbf{J}}(\mathbf{q}) = \tilde{\mathbf{E}}_\tau(\mathbf{q})\,. \tag{18}$$

Transforming back to the space domain and taking into account that $\mathbf{q} \to j\nabla_\tau$, where $\nabla_\tau = \mathbf{x}_0 \frac{\partial}{\partial x} + \mathbf{y}_0 \frac{\partial}{\partial y}$ is the tangential nabla operator, a differential equation for $\mathbf{J}$ is obtained

$$\frac{1}{\sigma}\left[\mathbf{J} + \frac{a}{4}\nabla_\tau^2 \mathbf{J} + a\left(b + \frac{1}{2}\right)\nabla_\tau \nabla_\tau \cdot \mathbf{J}\right] = \mathbf{E}_\tau\,. \qquad (19)$$

Equation (19) expresses the constitutive relation for graphene in the space domain, generalizing (5). Having been derived under the assumption of low wavenumbers, it will be accurate only for fields and currents with a sufficiently weak spatial variation. In theory, using (16) in (18) also leads to an equation for current density, which would be the extension of (19) for strong nonlocality. However, the q-dependence in σ_ϕ and ψ seems to preclude formulation of a tractable equation in purely differential form.

Assuming now a modal current as in (2), an integro-differential equation for $\mathbf{j}$ can be derived in the form

$$\begin{aligned}&\frac{1}{\sigma}\left[\mathbf{j} + \frac{a}{4}\left(\frac{\partial^2}{\partial x^2} - k_y^2\right)\mathbf{j}\right.\\&\left.\quad + a\left(b+\frac{1}{2}\right)\left(\mathbf{x}_0\frac{\partial}{\partial x} - jk_y\mathbf{y}_0\right)\left(\frac{\partial j_x}{\partial x} - jk_y j_y\right)\right] = \mathbf{e}_\tau\\&= -j\omega\int_\ell \underline{\tilde{\mathbf{G}}}_A(x-x';k_y)\cdot\mathbf{j}(x')\mathrm{d}x'\\&\quad + \frac{1}{j\omega}\left(\mathbf{x}_0\frac{\partial}{\partial x} - jk_y\mathbf{y}_0\right)\int_\ell \tilde{G}_\Phi(x-x';k_y)\nabla_\tau\cdot\mathbf{j}(x')\mathrm{d}x'.\end{aligned} \qquad (20)$$

Adopting the same MoM-Galerkin discretization scheme as in the previous section, the resulting matrix elements can be expressed as

$$\begin{aligned}Z_{ij} &= Z_{ij}^{\mathrm{loc}} + \frac{1}{\sigma}\int_\ell\left[-\frac{a}{4}k_y^2\mathbf{\Lambda}_i(x)\cdot\mathbf{\Lambda}_j(x) + \frac{a}{4}\mathbf{\Lambda}_i\cdot\frac{\partial^2\mathbf{\Lambda}_j}{\partial x^2}\right]\mathrm{d}x\\&- \frac{1}{\sigma}a\left(b+\frac{1}{2}\right)\int_\ell\left(\frac{\partial\Lambda_{ix}}{\partial x} + jk_y\Lambda_{iy}\right)\left(\frac{\partial\Lambda_{jx}}{\partial x} - jk_y\Lambda_{jy}\right)\mathrm{d}x\end{aligned} \qquad (21)$$

where $i,j = 1,\ldots,N$; the matrix elements $Z_{ij} = Z_{ij}^{\mathrm{loc}}$ obtained with the local formulation of Section II are of course recovered by letting $a = b = 0$.

IV. Results

The case of a single GNR is considered first for validation purposes. Dispersion results are reported for a GNR having width $w = 400$ nm, placed in free space at a distance $h = 50$ nm from the ground plane. In Fig. 4, the results obtained with the proposed spatial-MoM formulation based on the local conductivity model reported in Section II are compared with those obtained through a local spectral-domain formulation [10]; as it can be seen, a perfect agreement can be observed between the two formulations.

The same single-GNR configuration is then analyzed adopting the spatial-MoM formulation based on the weakly nonlocal conductivity model derived in Section III. The resulting dispersion curve is compared with that obtained through the local model and a spectral formulation which includes spatial-dispersion effects for arbitrary wavevector values [10]; the latter can be taken as a benchmark result, but it has been developed only for a single strip. This is illustrated in Fig. 5(a) and (b), where the normalized phase and attenuation constants are

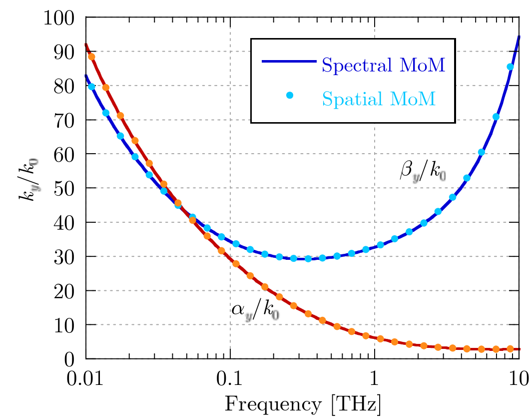

Fig. 4. Dispersion properties of a grounded free-standing single GNR with $w = 400$ nm: comparison between a spatial-MoM and a spectral-MoM formulation in the local approximation.

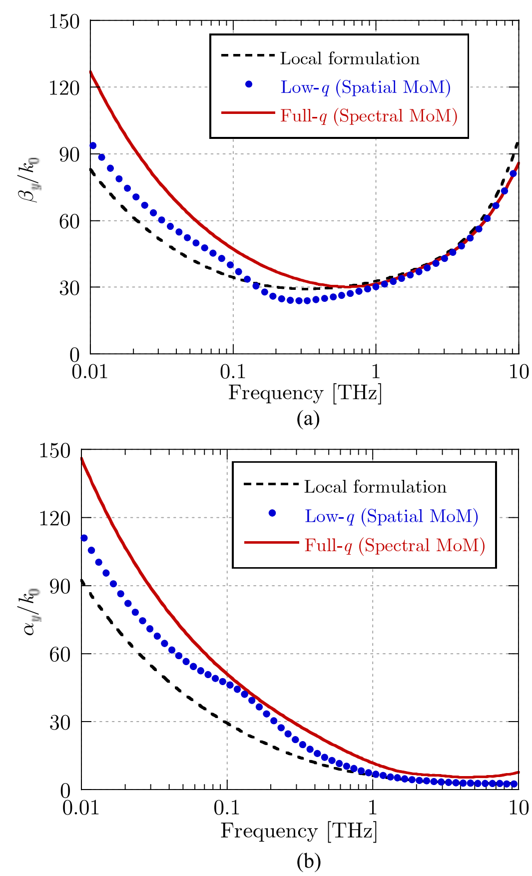

Fig. 5. Normalized phase (β/k_0) and attenuation (α/k_0) constants for the fundamental mode supported by the grounded free-standing GNR considered in Fig. 4 adopting different formulations.

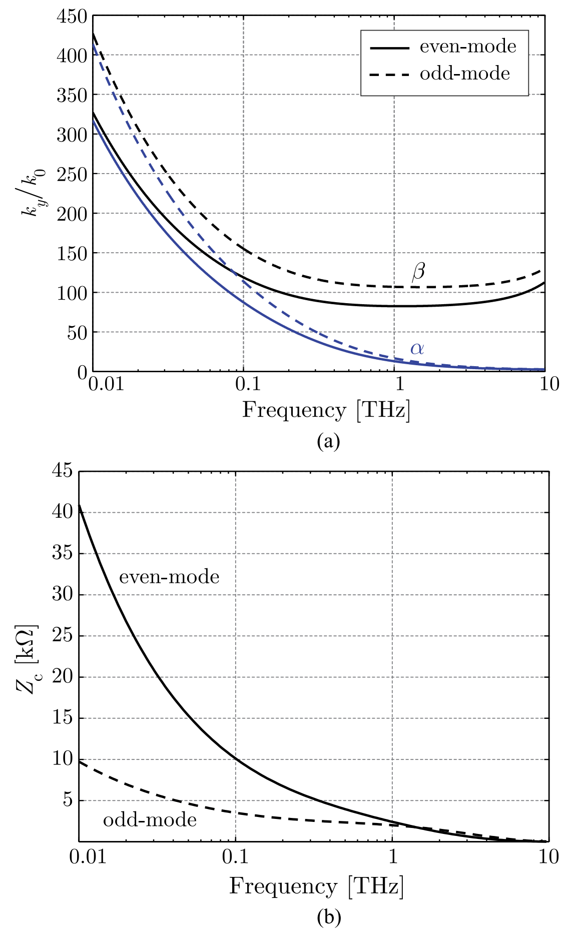

Fig. 6. (a) Normalized phase (β/k_0) and attenuation (α/k_0) constants and (b) characteristic impedance calculated according to a power-current definition, for the fundamental even and odd modes supported by two identical grounded coupled GNRs. *Parameters*: $w = 100$ nm, $h = 20$ nm, $s = 20$ nm.

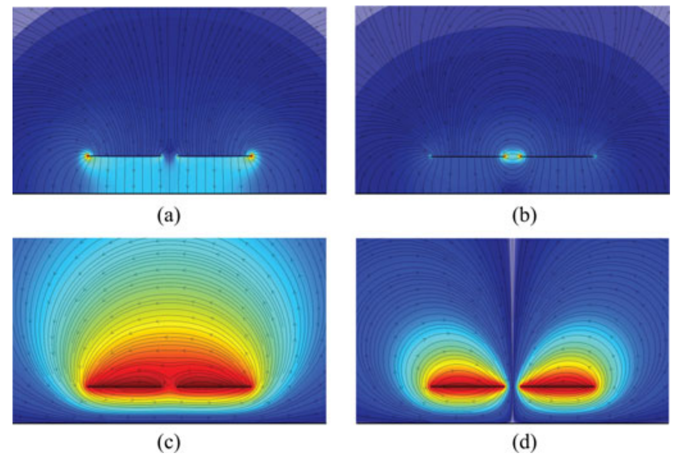

Fig. 7. Maps of the electric and magnetic field patterns, for the two relevant modes, at the frequency of 1 THz. (a) Pattern of E-field of the even mode. (b) Pattern of E-field of the odd mode. (c) Pattern of H-field of the even mode. (d) Pattern of H-field of the odd mode.

reported as functions of frequency. As it can be seen, strong spatial-dispersion effects occurr at low frequencies, where the low-q formulation furnishes a better representation with respect to the purely local model. It is worth noting that, while the spectral-domain approach can easily handle strong nonlocal effects, the spatial-domain formulation allows for efficiently treating nanoribbons with wide transverse separations and can easily be extended in order to have a self-consistent method allowing for the chemical potential to vary across the strip (i.e., a nonhomogeneous conductivity), or for “creating” a strip by suitably biasing a uniform sheet [21].

Let us now consider a multiconductor configuration constituted by a pair of identical coupled GNRs with strip width $w = 100$ nm and spacing $s = 20$ nm, placed in free space at a distance $h = 50$ nm from the ground plane. In Fig. 6(a), dispersion and attenuation curves are reported for the fundamental even and odd modes supported by the considered coupled GNRs over a ground plane in a wide frequency range, calculated with the spatial-MoM formulation based on the *local* graphene conductivity model of Section II. The odd mode has substantially higher phase constant than the even mode and, hence, a higher transverse confinement, for frequencies below 10 THz. However, below 1 THz, its attenuation constant is also substantially larger. A number $N = 23$ of basis functions in (6) has been considered.

In Fig. 6(b), the real part of the characteristic impedances Z_C of the same modes (which is the dominant part, especially at high frequencies, where applications are sought) is reported. These have been calculated according to a power-current definition; as expected, Z_C is higher for the even mode for frequencies below 10 THz, and for both modes it is in the range of tens of kilohm, which is the common order of magnitude for these kind of nanostructures [22].

The patterns of the electric and magnetic fields of the fundamental even and odd modes are reported in Fig. 7 at the frequency of 1 THz. They show the usual features typical of the TEM or quasi-TEM modes in standard metal coupled microstrip lines, with a clear confinement of the modes near the GNRs.

The same structure as in Fig. 6 is now simulated with the spatial-MoM formulation based on the *weakly nonlocal* graphene conductivity model of Section III. In Fig. 8, a comparison is reported between the local and weakly nonlocal spatial-MoM results for dispersion and attenuation features of the fundamental even and odd modes. It can be noted that in both cases, the local model is quite accurate up to the terahertz regime, although the weakly nonlocal model furnishes a slight correction (few percent) to the purely local results.

In Fig. 9, the same comparison is reported for the relevant characteristic impedances (in particular, the real parts). It can be noted that in this case, the spatial dispersion greatly affects the values of Z_c. In fact, while its effect on the propagation constants of the modes is of limited importance, it changes the modal current profiles and the modal field patterns in such a way that the computation of the characteristic impedance (based on a power-current definition) is strongly modified; in fact, both the values and the frequency behavior are different in the purely local and in the weakly nonlocal cases. In particular, it can be

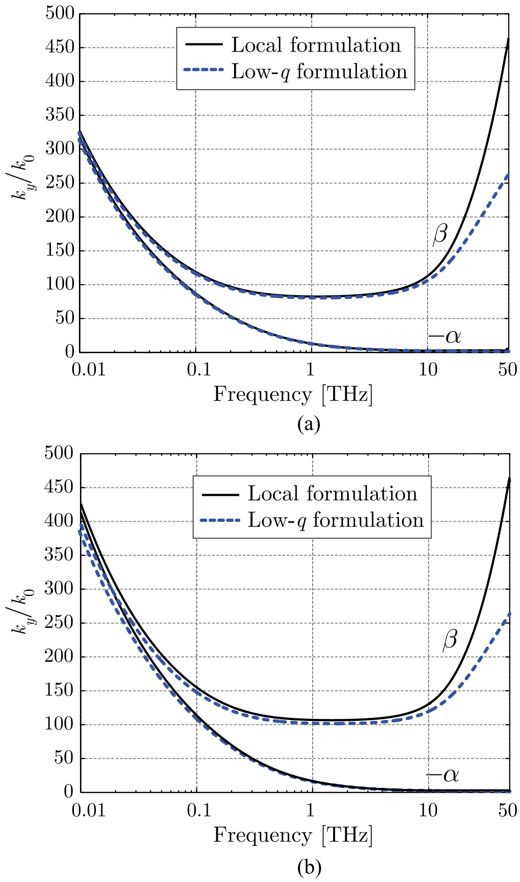

Fig. 8. Comparison between local and weakly nonlocal spatial-MoM formulations: Normalized phase (β/k_0) and attenuation (α/k_0) constants for the (a) fundamental even and (b) odd modes supported by the structure considered in Fig. 6.

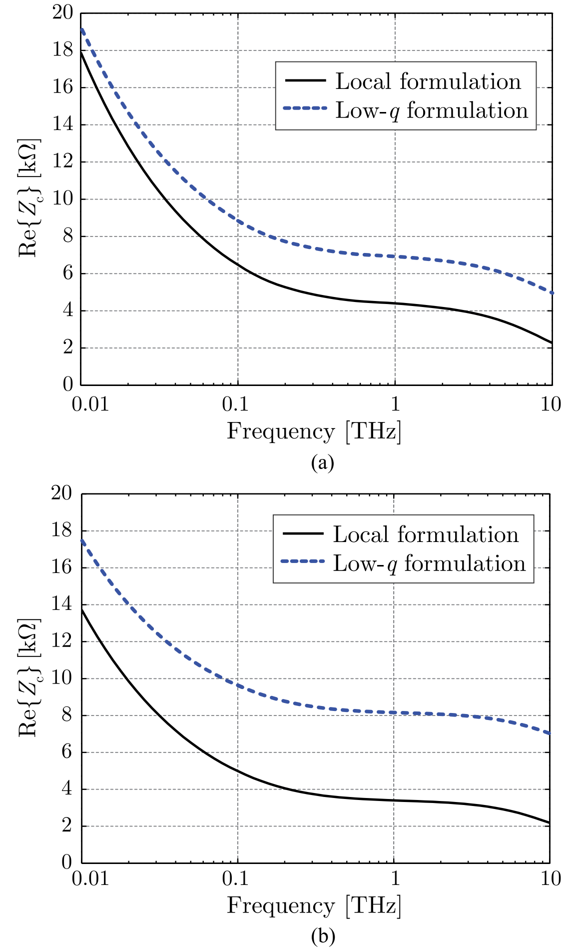

Fig. 9. Comparison between local and weakly nonlocal spatial-MoM formulations: (a) Even-mode and (b) odd-mode real-part characteristic impedances for the same structure considered in Fig. 6.

seen that the presence of spatial dispersion maintains the values of the characteristic impedances in the range of kilohm also in the high-frequency regime.

Once the frequency behavior of the wavenumbers and characteristic impedances of the even and odd modes are available, the crosstalk between two coupled GNRs can be computed straightforward. Given, the transformation matrix $\underline{\mathbf{T}}$ defined as

$$\underline{\mathbf{T}} = \begin{bmatrix} 0.5 & 0.5 \\ 0.5 & -0.5 \end{bmatrix} \tag{22}$$

the actual currents $\mathbf{I} = [I_1, I_2]^t$ and voltages $\mathbf{V} = [V_1, V_2]^t$ can be expressed in terms of modal currents $\mathbf{I}_\mathrm{m} = [I_\mathrm{even}, I_\mathrm{odd}]^t$ and voltages $\mathbf{V}_\mathrm{m} = [V_\mathrm{even}, V_\mathrm{odd}]^t$ as [14]

$$\mathbf{I} = \underline{\mathbf{T}}\mathbf{I}_\mathrm{m} \tag{23a}$$

$$\mathbf{V} = \underline{\mathbf{T}}^{-1}\mathbf{V}_\mathrm{m}\,. \tag{23b}$$

Therefore, the solution of the coupled GNRs reduces to the solution of two equivalent uncoupled single-wire transmission lines, for the even and odd modes, respectively, whose propagation constant and characteristic impedance are known (the same approach can be used when more than two GNRs are considered, resorting to a standard multiconductor transmission-line analysis [14]). In particular, to study crosstalk, we consider the circuit in Fig. 10; the coupled microstrip lines are identical to those in Fig. 1, except that they are of finite length $\ell = 2\,\mu$m. As shown, line #1 (source line) is fed with a voltage generator E_S1, at $y = 0$, and all four ports are terminated with the same impedance Z_load, i.e., $Z_\mathrm{S1} = Z_\mathrm{L2} = Z_\mathrm{L3} = Z_\mathrm{L4} = Z_\mathrm{load}$, which is equal to the diagonal elements of the characteristic matrix $\mathbf{Z}_\mathrm{c}$, i.e., $Z_\mathrm{load} = Z_\mathrm{c11} = Z_\mathrm{c22}$. We label the driven and terminated ends of line #1 as ports 1 and 2, while the near and

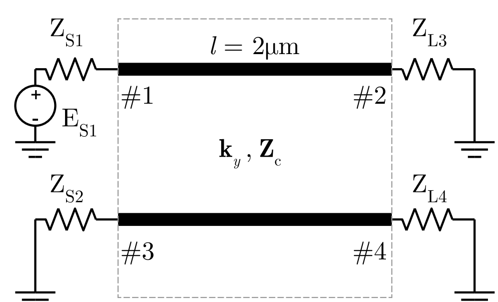

Fig. 10. Coupled GNR configuration considered for crosstalk analysis.

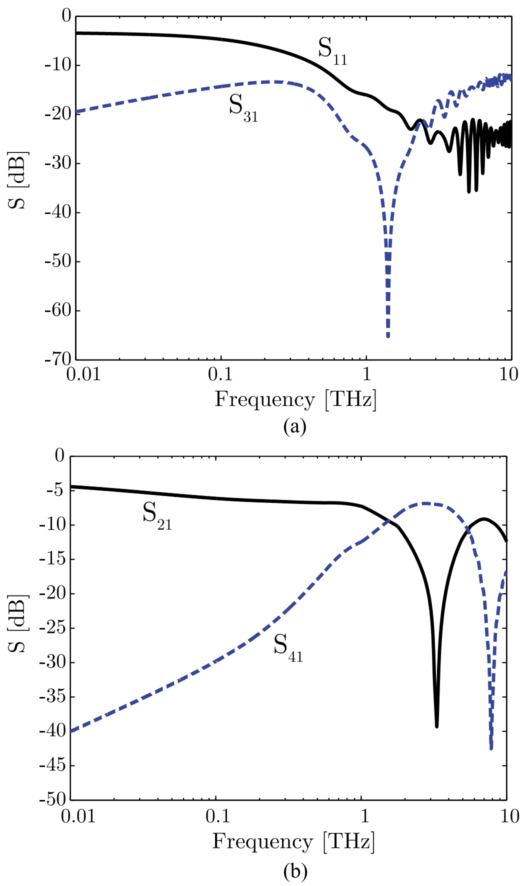

Fig. 11. Frequency spectra of the near- and far-end crosstalk for a configuration as in Fig. 10; the GNRs are simulated using a *local* conductivity model.

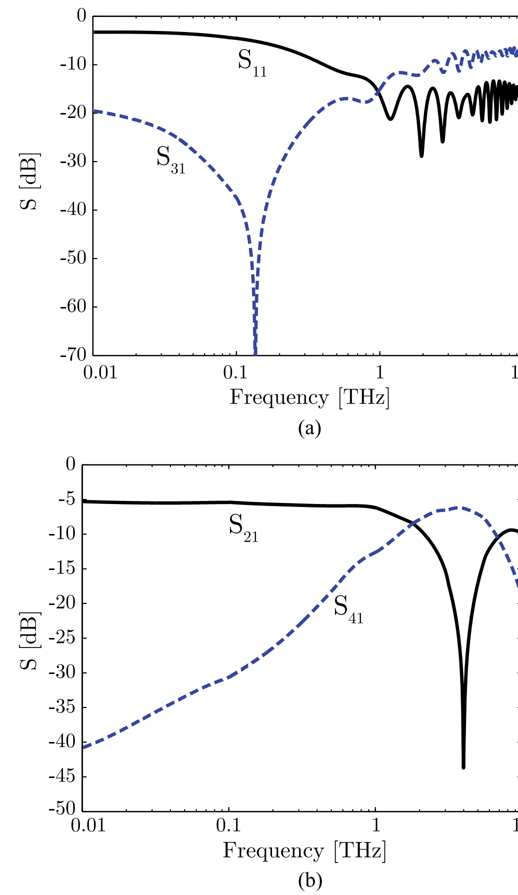

Fig. 12. Frequency spectra of the near- and far-end crosstalk for a configuration as in Fig. 10; the GNRs are simulated using a *weakly nonlocal* conductivity model (a) Near End (b) Far End.

far ends of line $\#2$ (victim line) as ports 3 and 4, respectively. The near- and far-end crosstalk can be related to the S parameters [15] that can be computed through the traveling forward and backward power waves a and b, respectively, defined at each port as [23], [24]

$$a\left(Z_{\mathrm{ref}}\right) = \frac{V + Z_{\mathrm{ref}} I}{2\sqrt{\mathrm{Re}\{Z_{\mathrm{ref}}\}}} \tag{24a}$$

$$b\left(Z_{\mathrm{ref}}\right) = \frac{V - Z_{\mathrm{ref}}^{*} I}{2\sqrt{\mathrm{Re}\{Z_{\mathrm{ref}}\}}} \tag{24b}$$

where Z_{ref} is the reference impedance, taken equal to the Z_{load}, the symbol * stands for complex conjugate, and V and I are the complex phasors of the voltage and current at the port, respectively (the sign of the current is positive when entering into the coupled lines). Once the power waves are available, it is immediate to compute the relevant elements of the scattering matrix as

$$S_{i1} = \frac{b_i\left(Z_{\mathrm{ref}}\right)}{a_1\left(Z_{\mathrm{ref}}\right)}, \quad i = 1, 2, 3, 4 \tag{25}$$

and obtain the whole scattering matrix applying the relevant properties dictated by reciprocity, i.e., $S_{ij} = S_{ji}$, and symmetry, i.e., $S_{ii} = S_{jj}$.

The crosstalk results are reported in Fig. 11 for a local conductivity model, and in Fig. 12 for a weakly nonlocal conductivity model, respectively, in the frequency range from 10 GHz up to 10 THz. The S-parameter formalism, usually employed to describe the microwave properties of interconnects, offers a natural way of describing crosstalk also in the terahertz range. Looking at both the near- and far-end crosstalk, several observations are possible, keeping in mind that backward propagating crosstalk (i.e., S_{31}) is usually the sum of capacitive and inductive coupling between the interconnects while forward propagating crosstalk (i.e., S_{41}) is the difference between capacitive and inductive coupling. Starting from 10 GHz, we observe that the magnitude of S_{31} is higher than S_{41}, denoting a weak coupling between the lines. By increasing frequency, the far-end noise increases steadily, denoting a more and more tight coupling and an opposite polarity between the capacitive and inductive couplings. In the range around 1.5 THz, the near-end noise presents a sharp antiresonance and the far-end noise presents a range of maximum. This can be understood reminding that the far-end crosstalk can be considered as an effect caused by the difference in velocity between the odd and even modes of propagation and, thus, a difference in edge arrival times at the end of the victim line. By observing Fig. 8, it can be seen that in this range the two modes reach their higher propagation velocities and that the attenuation constants are very low; hence, the difference between the two velocities is very significant in this range. It is worthy to observe that, where the far-end crosstalk is maximum, the insertion loss (i.e., $-S_{21}$) presents a maximum too, confirming a tight coupling between the lines with a high transfer of energy from the aggressor to the victim line. Also the increase of the input return loss (i.e., $-S_{11}$) above 1 THz, confirms this scenario.

When the low-q formulation is adopted, the above observations are still valid, with a tight coupling between lines shifted around 3 THz where, as shown in Fig. 12(b), the forward crosstalk and the insertion loss present a maximum. However, it is worth noting that the inclusion of spatial dispersion in the graphene conductivity moves drastically the antiresonance in the backward crosstalk from 1.5 to 0.2 THz, with a shift of almost a decade. This can be explained by observing that the higher values of the characteristic impedances caused by the spatial dispersion (as already noted about Fig. 9) increase the distributed per unit length mutual inductance and capacitance which, at lower frequencies (in this case around 0.2 THz) are in antiresonance, resulting in a large increase in the suppression of noise.

V. Conclusion

A two-step numerical procedure for the crosstalk analysis in GNR configurations has been presented. First, the relevant modal quantities are calculated with a full-wave approach based on the MoM in the spatial domain, then an equivalent modal circuit is extracted and considered for a standard modal analysis.

The spatial-domain approach is particularly suitable for the analysis of multiple-GNR configurations, since it is numerically efficient for large GNR spacings and also allows for modeling possible spatial inhomogeneities of the GNR conductivity, which can in turn help in synthesizing the desired modal behaviors. Two spatial-domain formulations have been presented, based on different conductivity models for graphene, namely a scalar local model and a tensor weakly nonlocal model. Results have been presented to validate the proposed approaches and illustrate crosstalk features for pairs of identical GNRs above a ground plane confirming that spatial-dispersion effects can be important in GNR applications and have to be carefully addressed.

References

[1] M. D'Amore, M. S. Sarto, G. W. Hanson, A. Naeemi, and B. K. Tay, "Special issue on applications of nanotechnology in electromagnetic compatibility (nano-EMC)," *IEEE Trans. Electromagn. Compat.*, vol. 54, no. 1, pp. 2–5, Feb. 2012.

[2] G. W. Hanson, "Quasi-transverse electromagnetic modes supported by a graphene parallel-plate waveguide," *J. Appl. Phys.*, vol. 104, art. no. 084314, 2008.

[3] G. W. Hanson, "Dyadic Green's function and guided surface waves for a surface conductivity model of graphene," *J. Appl. Phys.*, vol. 103, art. no. 064302, 2008.

[4] C. Xu, H. Li, and K. Banerjee, "Modeling, analysis, and design of graphene nano-ribbon interconnects," *IEEE Trans. Electron Devices*, vol. 56, no. 8, pp. 1567–1578, Aug. 2009.

[5] Y.-M. Lin, A. Valdes-Garcia, S.-J. Han, D. B. Farmer, I. Meric, Y. Sun, Y. Wu, C. Dimitrakopoulos, A. Grill, P. Avouris, and K. A. Jenkins, "Wafer-scale graphene integrated circuit," *Science*, vol. 332, no. 6035, pp. 1294–1297, Jun. 2011.

[6] A. Y. Nikitin, F. Guinea, F. J. García-Vidal, and L. Martín-Moreno, "Edge and waveguide terahertz surface plasmon modes in graphene microribbons," *Phys. Rev. B*, vol. 84, no. 16, art. no. 161407, Oct. 2011.

[7] R. Araneo, G. Lovat, and P. Burghignoli, "Dispersion analysis of graphene nanostrip lines," presented at the *IEEE Int. Symp. Antennas Propag. Soc.*, Chicago, IL, USA, 2012.

[8] G. Lovat, P. Burghignoli, and R. Araneo, "Low-frequency dominant-mode propagation in spatially-dispersive graphene nano-waveguides," *IEEE Trans. Electromagn. Compat.*, vol. 55, no. 1, pp. 101–109, Feb. 2013.

[9] G. Lovat, G. Hanson, R. Araneo, and P. Burghignoli, "Comparison of spatially dispersive models for dyadic intraband conductivity of graphene," in *Proc. Eur. Conf. Antennas Propag.*, Gothenburg, Sweden, 2013, pp. 500–504.

[10] G. Lovat, G. W. Hanson, R. Araneo, and P. Burghignoli, "Semiclassical spatially dispersive intraband conductivity tensor and quantum capacitance of graphene," *Phys. Rev. B*, vol. 87, no. 11, art. no. 115429, Mar. 2013.

[11] G. W. Hanson, "Dyadic Green's functions for an anisotropic non-local model of biased graphene," *IEEE Trans. Antennas Propag.*, vol. 56, no. 3, pp. 747–757, Mar. 2008.

[12] R. Araneo, C. Wang, X. Gu, S. Celozzi, and J. Drewniak, "Differential signalling in PCBs: Modeling and validation of dielectric losses and effects of discontinuities," in *Proc. IEEE Int. Symp. Electromagn. Compat.*, Montreal, Canada, 2001, vol. 2, pp. 933–938.

[13] R. Araneo, C. Wang, X. Gu, J. Drewniak, and S. Celozzi, "Efficient modeling of discontinuities and dispersive media in printed transmission lines," *IEEE Trans. Magn.*, vol. 38, no. 2, pp. 765–768, Mar. 2002.

[14] C. R. Paul, *Analysis of Multiconductor Transmission Lines*. New York, NY, USA: Wiley, 2008.

[15] D. Hill, K. Cavcey, and R. Johnk, "Crosstalk between microstrip transmission lines," *IEEE Trans. Electromagn. Compat.*, vol. 36, no. 4, pp. 314–321, Nov. 1994.

[16] P. Burghignoli, R. Araneo, G. Hanson, and G. Lovat, "Space-domain method of moments for graphene nanoribbons," in *Proc. Eur. Conf. Antennas Propag.*, The Hague, The Netherlands, 2014, pp. 666–669.

[17] R. Araneo, G. Lovat, S. Celozzi, and P. Burghignoli, "Crosstalk analysis in graphene MTLs," presented at the *IEEE Int. Symp. Electromagn. Compat.*, Raleigh, NC, USA, 2014.

[18] V. P. Gusynin, S. G. Sharapov, and J. P. Carbotte, "Magneto-optical conductivity in graphene," *J. Phys. Condens. Matter*, vol. 19, no. 2, art. no. 026222, Jan. 2007.

[19] C. Gillan, A. Schuchinsky, and L. Spence, "Computing zeros of analytic functions in the complex plane without using derivatives," *Comput. Phys. Commun.*, vol. 175, no. 4, pp. 304–313, Aug. 2006.

[20] R. Rodríguez-Berral, F. Mesa, and F. Medina, "Systematic and efficient root finder for computing the modal spectrum of planar layered waveguides," *Int. J. RF Microw. Comput. Eng.*, vol. 14, no. 1, pp. 73–83, Jan. 2004.

[21] E. Forati and G. W. Hanson, "Soft-boundary graphene nanoribbon formed by a graphene sheet above a perturbed ground plane: Conductivity profile and SPP modal current distribution," *J. Opt.*, vol. 16, no. 8, art. no. 089501, 2014.

[22] P. D. Nguyen, T. C. Nguyen, A. T. Huynh, and E. Skafidas, "High frequency characterization of graphene nanoribbon interconnects," *Mater. Res. Exp.*, vol. 1, no. 3, art. no. 035009, 2014.

[23] D. C. Youla, "On scattering matrices normalized to complex port numbers," *Proc. IRE*, vol. 49, art. no. 1221, 1961.

[24] K. Kurokawa, "Power waves and the scattering matrix," *IEEE Trans. Microw. Theory Tech.*, vol. 13, no. 2, pp. 194–202, Apr. 1965.

Authors' photographs and biographies not available at the time of publication.